

# Plume heat flow in a numerical model of mantle convection with moving plates

Masaki Yoshida <sup>a,\*</sup>, Masaki Ogawa <sup>b</sup>

<sup>a</sup> *The Earth Simulator Center, Japan Agency for Marine-Earth Science and Technology, 3173-25, Showa-machi, Kanazawa-ku, Yokohama, Kanagawa 236-0001, Japan*

<sup>b</sup> *Department of Earth Sciences and Astronomy, University of Tokyo, 3-8-1, Komaba, Meguro, Tokyo 153-8902, Japan*

Received 27 December 2004; received in revised form 26 August 2005; accepted 7 September 2005

Available online 10 October 2005

Editor: S. King

## Abstract

Self-consistent numerical models are presented for a two-dimensional thermal convection with moving plates to estimate the heat flow transported by hot upwelling plumes in both internally and basally heated mantle. The plume heat flow depends on the internal heating rate and convective regimes but does not exceed 30% of basal heat flow when the plates rigidly move as observed on the Earth; the fraction of plume heat flow to basal heat flow becomes higher when the lithosphere behaves as a stagnant lid or as a mechanically not so strong plate. When estimated from the dynamic topography of plume-swells above hot upwelling plumes, the plume heat flow appears to be only a small fraction of the real plume heat flow. As a whole, the apparent plume heat flow estimated from dynamic topography remains only a few percent of the total heat flow on the surface boundary, the value observed for the Earth, even when the basal heating rate exceeds 50% of the total heating rate. Such a high fraction of basal heating rate is necessary for the amplitude of topography above hot upwelling plumes to become comparable to the value observed for the Earth, too. It is necessary to reexamine the earlier inference that the heat released from the core manifests itself as plume heat flow in the Earth.

© 2005 Elsevier B.V. All rights reserved.

*Keywords:* mantle convection; numerical model; heat flow; mantle plume; moving plate; topography

## 1. Introduction

The hot upwelling plumes as manifested by hotspot volcanoes [1] transport heat and mass from deep mantle to the base of the lithosphere and induce topographic high called hotspot-swell [2,3]. Davies [2] and Sleep [3] have estimated the amount of heat transported by the hot upwelling plumes from the volume of hotspot-swells and conclude that the plume heat flux is less

than 6% of the total amount of heat that the Earth's mantle is losing, 36 TW [4]. Davies [2,5] has further suggested that this plume heat flux is all coming from the core. Indeed, the estimated plume heat flux is comparable to the heat flux at the core–mantle boundary suggested in many of the recent studies of geodynamo (for a review, see [6]) and thermal history of the core [7–9]. Based on the estimated plume heat flux, Davies [2,5] has also suggested that the solid-state convection in the Earth's mantle is mostly driven by internal heating and that the contribution of basal heating is minor.

\* Corresponding author.

*E-mail address:* [myoshida@jamstec.go.jp](mailto:myoshida@jamstec.go.jp) (M. Yoshida).

This “classic” view of mantle convection is, however, not self-evident. Many of seismic tomographic images have suggested that the deeper part of the lower mantle is chemically heterogeneous with a spatial scale of 1000 km or more [10–13]. A numerical model of thermo-chemical convection in the mantle has shown that such chemically heterogeneous regions in deep lower mantle are dynamically stable for a geologic time even when the regions are enriched in heat producing elements [14]. In a chemically heterogeneous mantle, plumes can arise from local chemical boundaries as well as the core–mantle boundary as suggested from a laboratory experiment [15–17]. Recent seismic tomography images and geochemical evidence indeed suggest that not all of the hotspot plumes come from the core–mantle boundary [21,22].

Given the controversy on the origin of hot upwelling plumes, it is worth re-examining the constraint on the origin derived from the low apparent plume heat flux [2,5]. For the purpose to reexamine this, a couple of studies have been numerically studied using mantle convection models. Mittlestaedt and Tackley [19] have investigated the relationship between plume heat flow and CMB heat flow in steady-state or weakly time-dependent convection using two-dimensional Cartesian or axisymmetric models. They have concluded that the heat flow through the CMB may be several times larger than the heat carried by plumes. Labrosse [18] has carefully investigated this using a three-dimensional (3-D) Cartesian model in which the viscosity is spatially constant and the bottom heat flux is about 50% of the surface heat flux. He had found that plume heat flux is only a fraction of CMB heat loss, and CMB heat flux is strongly correlated to the arrival of downwellings at the CMB. Recently, using 3-D spherical shell model with depth- and temperature-dependent viscosity, Zhong [20] has found that both the ratios of plume heat flux to surface heat flux and bottom heat flux increase for a given amount of internal heating rate, and plume heat flux is more comparable to core heat flux.

In this paper, to confirm that their conclusions still apply with mantle convection with moving plates, we estimate plume heat flux for a series of numerical models of mantle convection with self-consistently reproduced moving plates driven by both internal and basal heating.

## 2. Model descriptions

We consider a thermal convection of infinite Prandtl number fluid in a two-dimensional rectangular box with

an aspect ratio of 5. Boussinesq approximation is employed. In the formulation of the basic equations governing the mantle convection, the length  $\tilde{L}$ , velocity  $\tilde{v}$ , time  $\tilde{t}$ , and temperature  $\tilde{T}$  are non-dimensionalized as,

$$\tilde{L} = \tilde{z}_1 L', \quad \tilde{v} = \frac{\tilde{\kappa}}{\tilde{d}} v', \quad \tilde{t} = \frac{\tilde{d}^2}{\tilde{\kappa}} t', \quad \tilde{T} = \Delta \tilde{T} T', \quad (1)$$

respectively, where  $\tilde{\kappa}$  is the thermal diffusivity,  $\Delta \tilde{T} (= \tilde{T}_{\text{bot}} - \tilde{T}_{\text{top}})$  is the temperature difference between the bottom ( $z_0=0$ ) and top ( $z_1=1$ ) surfaces. (Symbols with tildes and primes stand for dimensional and non-dimensional quantities, respectively.)

Dropping primes in the quantities hereafter, the non-dimensional continuity, momentum, and energy equations under this non-dimensionalization are,

$$\frac{\partial v_i}{\partial x_i} = 0, \quad (2)$$

$$-\frac{\partial p}{\partial x_i} + \frac{\partial}{\partial x_j} \left\{ \eta \left( \frac{\partial v_i}{\partial x_j} + \frac{\partial v_j}{\partial x_i} \right) \right\} + Ra T \delta_{iz} = 0, \quad (3)$$

$$\frac{\partial T}{\partial t} = \frac{\partial^2 T}{\partial x_i^2} - v_i \frac{\partial T}{\partial x_i} + H, \quad (4)$$

where  $x_i=(x,z)$  are Cartesian coordinates with  $z$  being the vertical axis ( $z=0$  at the bottom boundary, and  $z=1$  at the top boundary),  $\delta_{iz}$  Kronecher's delta,  $v_i$  velocity,  $p$  pressure,  $\eta$  viscosity,  $T$  temperature, and  $t$  is the time.

The Rayleigh number  $Ra$  is defined by  $Ra = \tilde{\rho}_0 \tilde{g} \tilde{\alpha} \Delta \tilde{T} \tilde{d}^3 / \tilde{\eta}_0 \tilde{\kappa}$ , where  $\tilde{\rho}_0$  is the reference density of mantle,  $\tilde{g}$  gravitational acceleration,  $\tilde{\alpha}$  thermal expansivity,  $\tilde{d}$  the thickness of the convecting layer, and  $\tilde{\eta}_0$  is the reference viscosity (see Eq. (5) below). We assume  $Ra = 2.52 \times 10^8$  as calculated from the dimensional values of the parameters shown in Table 1. The internal

Table 1  
Parameters used in this study

Symbols	Meanings	Values
$c_p$	Specific heat	$1.25 \times 10^3 \text{ J kg}^{-1} \text{ K}^{-1}$
$g$	Gravity acceleration	$9.8 \text{ m s}^{-2}$
$k$	Thermal conductivity	$4.1 \text{ W m}^{-1} \text{ K}^{-1}$
$T_{\text{top}}$	Top surface temperature	273 K
$T_{\text{bot}}$	Bottom surface temperature	1873 K
$T_{\text{ref}}$	Reference temperature	1573 K
$\Delta T$	Temperature difference	1600 K
$\alpha$	Thermal expansivity	$2.0 \times 10^{-5} \text{ K}^{-1}$
$\eta_0$	Reference viscosity	$1.0 \times 10^{20} \text{ Pa s}$
$\kappa$	Thermal diffusivity	$1.0 \times 10^{-6} \text{ m}^2 \text{ s}^{-1}$
$\rho_0$	Reference density	$3.3 \times 10^3 \text{ kg m}^{-3}$
$\rho_m$	Reference density of mantle	$3.3 \times 10^3 \text{ kg m}^{-3}$
$\rho_w$	Density of ocean water	$1.0 \times 10^3 \text{ kg m}^{-3}$
$\Delta \rho_{\text{top}}$	Density contrast at top surface	$2.3 \times 10^3 \text{ kg m}^{-3}$
	$(\rho_m - \rho_w)$	

heat source is uniform and the heating rate per unit volume  $H$  is non-dimensionalized by  $H \equiv \tilde{d}^2 \tilde{H} / \tilde{\kappa} \tilde{c}_p \Delta \tilde{T}$ , where  $\tilde{H}$  is the internal heating rate per unit mass, and  $\tilde{c}_p$  is specific heat;  $H$  is varied in the range of 0 to 22 in this study.

To make the thermal boundary layer along the top surface boundary show a plate-like behavior, we introduce a “damage parameter”  $\omega$ , which represents the “degree of damage”, into the viscosity equation [23–25]. The viscosity of convecting materials depends on  $\omega$  as well as temperature and depth [23] as

$$\eta = \exp \left[ -E(T - T_{\text{ref}}) + V(1 - z) - F \frac{\omega}{\omega + 1} \right], \quad (5)$$

where  $E$ ,  $V$  and  $F$  are constants, and the reference temperature  $T_{\text{ref}}$  is taken as 0.8125 ( $\tilde{T}_{\text{ref}}=1573$  K in dimensional value), a characteristic temperature in the uppermost mantle when  $\Delta \tilde{T}$  is taken as 1873 K;  $E$  is varied in the range of 13 to 24 in this study. The constant  $V$  is fixed at  $\ln 10^{2.0}=4.61$ , which implies that there is a viscosity contrast of 100, comparable to the value appropriate for the Earth’s mantle (e.g., [26,27]), between the top and bottom boundaries of convecting box owing to the pressure effect. The constant  $F$  is fixed at  $\ln 10^{5.0}=11.51$ , which implies that the viscosity contrast of  $10^5$  arise between regions with  $\omega=0$  (no damage) and regions with  $\omega \rightarrow \infty$  (highly damaged).

The time evolution of  $\omega$  is governed by,

$$\frac{\partial \omega}{\partial t} + v_i \frac{\partial \omega}{\partial x_i} = \Gamma \tau_{ij} \epsilon_{ij} - \omega \lambda_0 \exp(ET), \quad (6)$$

where  $\tau_{ij}$  is stress,  $\epsilon_{ij}$  strain-rate,  $\Gamma$  constant (see below),  $1/\lambda_0$  is the healing time at  $T=0$  taken to be  $1/\lambda_0=10^{-5}$  [23]. Eq. (6) implies that the lithosphere is damaged in the regions where viscous dissipation rate is high and recovers from the damage with the healing time, which depends on temperature. When scaled to the Earth, the healing time at  $T=0$  is  $10^6$  years, much shorter than the turnover time of mantle convection,  $\sim 10^8$  years. The healing time decreases with increasing temperature.

Because of the short healing time, the steady state assumption holds well in most situations, that is, the left-hand side of Eq. (6) is negligible [23]. Namely,

$$\frac{\tau^2 \Gamma}{\lambda_0 \eta^\dagger} = \omega \exp \left( -F \frac{\omega}{\omega + 1} \right), \quad (7)$$

where  $\eta^\dagger = \exp[ET_{\text{ref}} + V(1 - z)]$ , and  $\tau$  is the second invariant of deviatoric stress. Fig. 1 illustrates the rela-

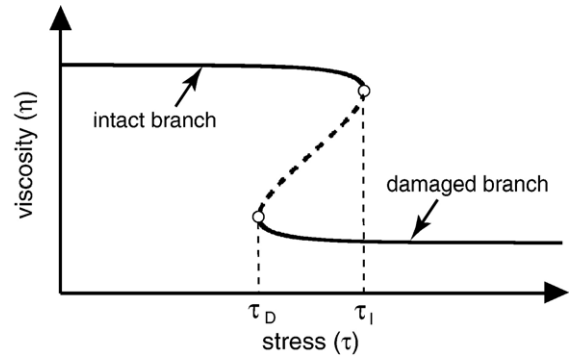


Fig. 1. The convecting fluid selects one of the two branches indicated by the solid parts of the curve, i.e., intact branch or damaged branch, depending on the stress-history that the fluid has experienced in the past. The dashed part of the curve is physically unrealizable.

tionship of stress  $\tau$  and viscosity  $\eta$  calculated from Eq. (6) with  $F=11.51$ . There is a hysteresis in the  $\tau$ – $\eta$  relationship in the stress range of  $(\tau_D, \tau_I)$  calculated from  $\eta^\dagger$ ,  $F$ ,  $\lambda_0$  and  $\Gamma$  (see Fig. 1 and [23]), and the convecting fluid selects one of the two branches in the stress range depending on the stress-history that the fluid has experienced. The hysteresis plays a crucial role in inducing a plate-like behavior of the numerically modeled lithosphere. Narrow plate margins, which are on the damaged branch characterized by  $\omega \gg 1$  and low viscosity (see Fig. 1), develop within the lithosphere to divide it into rigidly moving smaller pieces or “plates”, which are on the intact branch characterized by  $\omega \ll 1$  and high viscosity, when the stress induced in the lithosphere by ridge push force is within the stress range.

As shown in Fig. 1,  $\tau_I$  is the maximum stress on the intact branch and corresponds to the rupture strength of plates in the Earth. The rupture strength of the Earth’s plates has been estimated to be on the order of 100 MPa [28]. On the other hand,  $\tau_D$  is the minimum stress on the damaged branch and corresponds to the mechanical strength of plate margins and may be estimated from the stress drop of shallow earthquakes, which is on the order of 1 MPa [29]. The estimate of  $\tau_D$  and  $\tau_I$  suggests that  $\Delta \tau \equiv \tau_I / \tau_D$  for the Earth is on the order of 100. From Eq. (7), when  $F = \ln 10^{5.0}$ , it can be shown that the stress contrast  $\Delta \tau$  is 11.1. Although the adopted value of  $\Delta \tau$  may be an order of magnitude smaller than the realistic value, it is sufficient to make the numerically modeled lithosphere show a plate-like behavior. To make  $\tilde{\tau}_I$  and  $\tilde{\tau}_D$  in the numerical model close to the values appropriate for the Earth, we assume that  $\Gamma = 2.0 \times 10^{-5}$ . The adopted value of  $\Gamma$  implies that  $\tilde{\tau}_I \approx 10$ –500 MPa, and  $\tilde{\tau}_D \approx 1$ –50 MPa (see Eq. (7) in [23]).

The adopted boundary conditions are as follows: The top and bottom boundaries are impermeable, shear stress-free, and isothermal ( $T_{\text{top}}=0$  at  $z=1$  and  $T_{\text{bot}}=1$  at  $z=0$ ). The vertical side-walls are reflecting, i.e., impermeable, shear stress-free, and adiabatic. The boundary condition for  $\omega$ -field (the distribution of the  $\omega$ ) is no-flux at all of the boundaries.

The basic equations are discretized by the finite volume method on a staggered grid and are solved by the use of stag3d [30] modified for this study. The explicit time-stepping method, MPDATA scheme with a second-order time accuracy, is used for the calculation of advection terms in the energy equation and the damage parameter equation. The diffusion term in the energy equation is calculated by a second-order finite difference method. The healing term in Eq. (6) is implicitly treated. As the initial condition for the energy equation and damage parameter equation, we adopt the temperature- and  $\omega$ -fields of  $T=0.5+0.01\cos(2\pi x)\sin(\pi z)$  and  $\omega=0$ , respectively, or the temperature- and  $\omega$ -fields obtained from previous calculations. The number of mesh points is 512 in the horizontal direction and is 80 in the vertical direction. The horizontal grid intervals are uniform, but the vertical grid intervals are non-uniform with higher resolution around the lower and upper thermal boundary layers.

In all of the cases described below, we continued calculations till the time-series of average heat flux on the top surface boundary and the root-mean-square velocity and average temperature in the entire convecting domain reach their statistically steady values.

### 3. Regime diagram

As a premise to the study of heat transport by hot upwelling plumes beneath moving plates, we first clarified the regime diagram of the thermal convection formulated above on the plane of internal heating rate  $H$  and the magnitude of temperature-dependence of viscosity  $E$ . The result is presented in Fig. 2. Fig. 2a classifies the numerically obtained convective flow patterns into the stagnant lid, plate-like, and weak plate regimes, all defined in [23].

In the weak plate regime at small  $E$ , the lithosphere is frequently damaged both by its own weight and by hot upwelling plumes, so that convection cells of aspect ratio about one develop (Fig. 2b), while in the stagnant lid regime at large  $E$ , the lithosphere behaves as a stagnant lid that never subducts (Fig. 2e). In the plate-like regime at moderate  $E$  and small  $H$ , in contrast, highly damaged narrow “plate margins” develop in the lid, each piece of the lid (i.e., “plate”) separated

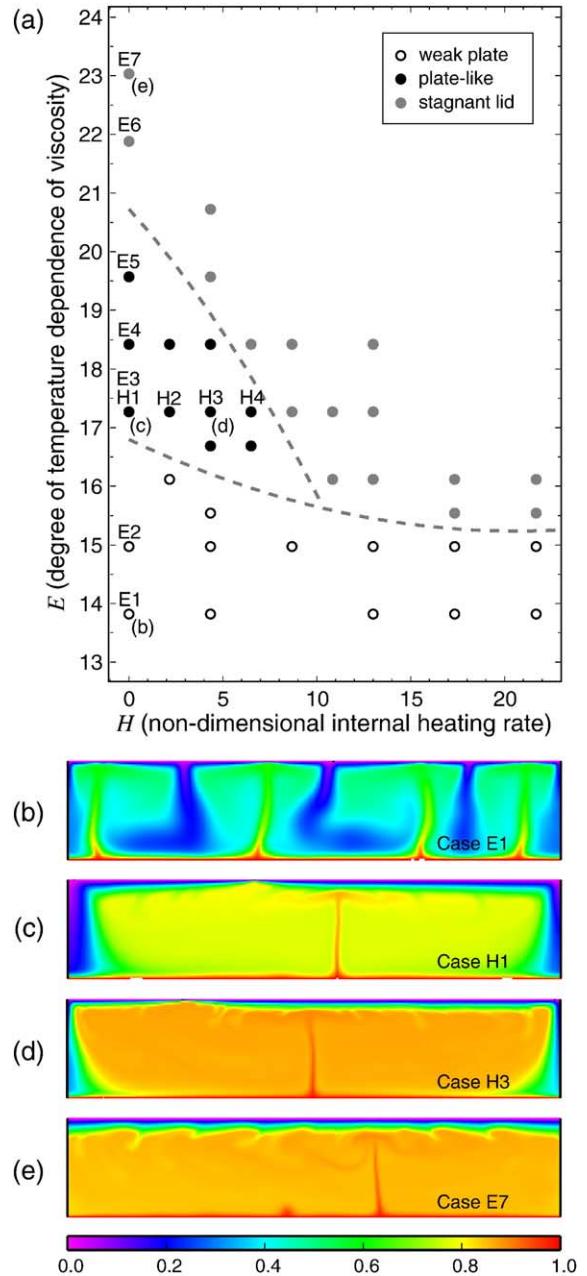


Fig. 2. (a) A regime diagram on the plane of the internal heating rate  $H$  and the magnitude of temperature-dependence of viscosity  $E$ . The convective flow patterns are classified into three regimes; the weak plate regime, the plate-like regime, and the stagnant lid regime, indicated by solid open circles, solid black circles, and solid gray circles, respectively. The regime boundaries shown by dotted lines are approximately derived using linear-least-square approach. (b)–(e) Selected snapshots of the temperature field for the cases shown in (a).

by the plate margins rigidly moves, and the plates induce convection cells of large aspect ratio (Fig. 2c and d). These features of convecting flow patterns and

the locations of regime boundaries at  $H=0$  are consistent with the earlier findings [23].

In this regime diagram, the upper limit of  $E$ , and hence the upper limit of the viscosity in the lithosphere, for the plate-like regime rapidly decreases with increasing  $H$ . This occurs because the temperature in the isothermal cores of convection cells increases, the excess temperature of hot upwelling plumes decreases, and hence, the buoyancy of hot upwelling plumes becomes weaker with increasing  $H$ . When the plume buoyancy becomes weaker than a threshold, hot plumes no longer break the lithosphere to form new plate margins. Under the circumstance, the plate-like motion stops in the present model when ridges and subduction zones merge and all of the plate margins happen to disappear. The plate-like behavior of lithosphere continues long only when there are agents, outside of the lithosphere, that occasionally destroy the lithosphere and develop new plate margins in the present model [23]. As a result of the rapid decrease in  $E$  at the boundary between stagnant lid and plate-like regimes with increasing  $H$ , the plate-like regime disappears and a bifurcation directly occurs between the weak plate regime and the stagnant lid regime when  $H$  is larger than about 10.

#### 4. Plume heat flow

We now estimate the flux of heat transported by hot upwelling plumes for all of the cases shown in Fig. 2 and study how the plume heat flow depends on the style of the convection and basal heating rate. In this section, all of the quantities are dimensional unless otherwise mentioned.

##### 4.1. Procedures for the estimate of plume heat flow

The plume heat flow  $Q_p$  is defined as,

$$Q_p = \sum_{\text{hot plumes}} \rho_0 c_p \int_{z=\text{const.}} v_z \Delta T_{\text{plume}} dx, \quad (8)$$

where  $\Delta T_{\text{plume}} = T_p - \langle T_m \rangle$  is the excess temperature of the hot upwelling plumes in which  $T_p$  is the temperature of plumes and  $\langle T_m \rangle$  is the averaged temperature of mantle removed the up/downwelling plumes,  $v_z$  is the vertical velocity of the hot upwelling plumes, the integration is carried out over the cross-sectional area of a plume tail, and the summation is taken for all of the hot plume tails. There are two possible ways to estimate  $Q_p$  for the numerically obtained flow patterns. One is to directly use Eq. (8). We carried out the integration of Eq. (8) at  $z=0.5$  and located plume boundaries along

the horizontal line of  $z=0.5$  as the points where  $|dT/dx|$  takes maximum. Another is to indirectly estimate  $Q_p$  from dynamic topography induced by the hot upwelling plumes, so-called, “plume-swell” as has been done for the Earth [2,3]. The basic assumption of this method is that the excess mass of plume-swell is balanced by the mass deficit of hot upwelling plumes,

$$\Delta \rho_{\text{top}} v_{\text{plate}} \delta h_{\text{swell}} g = \Delta \rho_{\text{plume}} v_z S_{\text{plume}} g, \quad (9)$$

where  $\Delta \rho_{\text{top}}$  is density contrast at the top boundary of convecting layer, i.e., between the mantle and oceanic water,  $v_{\text{plate}}$  the velocity of the plate over-laying the plume,  $\delta h_{\text{swell}}$  the swell height,  $\Delta \rho_{\text{plume}}$  density difference between the plume and the surrounding mantle,  $v_z$  the average vertical velocity of the upwelling plumes, and  $S_{\text{plume}}$  is the thickness of the plume [4,31,32]. (As discussed in [33], this assumption does not always hold and we will discuss the validity of the assumption for our model later.) When the plume buoyancy is strictly thermal, the density difference  $\Delta \rho_{\text{plume}} = \rho_m \alpha_0 \Delta T_{\text{plume}}$ . Hence, the plume heat flow estimated by plume-swell  $Q_s$  is calculated from the dynamic topography as

$$Q_s = \frac{c_p}{\alpha} \Delta \rho_{\text{top}} v_{\text{plate}} \delta h_{\text{swell}}. \quad (10)$$

Therefore the plume heat flow can be estimated from the plate velocity  $v_{\text{plate}}$  and the swell height  $\delta h_{\text{swell}}$ .

##### 4.2. Results

###### 4.2.1. Effects of internal/basal heating rate on plume heat flow

To show how the plume heat flow  $Q_p$  in Eq. (8) depends on the internal heating rate  $H$  and the basal heating rate, we present in Fig. 3a the plots of  $Q_p$ , the heat flow at the top boundary  $Q_t$ , and the heat flow at the bottom boundary  $Q_b$ , all against  $H$  for the cases H1 to H4 indicated in Fig. 2. All of the cases are in the plate-like regime and are calculated at  $E = \ln 10^{7.5} = 17.27$  or at the viscosity contrast between the lithosphere and asthenosphere of about  $10^6$ , a reasonable value for the Earth [34]. We will show in Section 4.2.2 below that the numerical results are hardly affected by the choice of  $E$  in the plate-like regime. The estimates of plume heat flow in Fig. 3a are calculated as an average of the estimates obtained from several snapshots of convective flow pattern during the runs.

The calculated plume heat flow  $Q_p$  is only 14–29% of the heat flow at the bottom boundary  $Q_b$ , and is 9–29% of the heat flow at the surface boundary  $Q_t$  in the plate-like regime shown in Fig. 3b. In contrast to the significant increase in top surface heat flow  $Q_t$

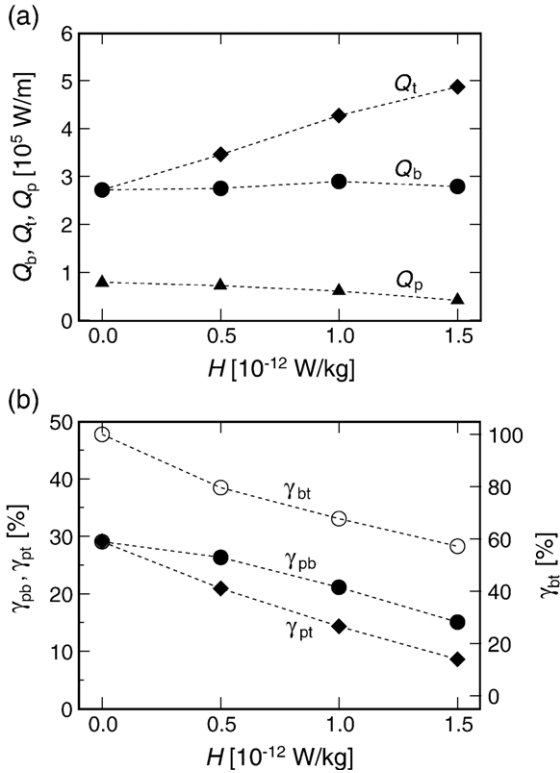


Fig. 3. Plots of the directly estimated plume heat flow for cases H1–H4 shown in Fig. 2. (a) The internal heating rate  $H$  versus the heat flow on the bottom boundary ( $Q_b$ , solid circles), the heat flow on the top surface boundary ( $Q_t$ , solid diamonds), and the plume heat flow ( $Q_p$ , solid triangles). (b) The ratio of  $Q_b$  to  $Q_t$  ( $\gamma_{bt}$ , open circles), the ratio of  $Q_p$  to  $Q_b$  ( $\gamma_{pb}$ , solid circles), and the ratio of  $Q_p$  to  $Q_t$  ( $\gamma_{pt}$ , solid diamonds) versus  $H$ .

with increasing  $H$ , the plume heat flow  $Q_p$  gently decreases with increasing  $H$ . This occurs because the iso-thermal core temperature of the mantle increases, and hence the excess temperature of plumes  $\Delta T_{\text{plume}}$  decreases with increasing  $H$  (see Eq. (8)). Fig. 3 also shows that the basal heat flow  $Q_b$  remains nearly constant. This occurs because the effects of smaller temperature contrast across the bottom thermal boundary layer is offset by the effects of thinner thermal boundary layer, both of which occur as  $H$  increases. Consequently,  $\gamma_{pb} \equiv Q_p/Q_b$  and  $\gamma_{pt} \equiv Q_p/Q_t$  decrease with increasing  $H$  (Fig. 3b).

#### 4.2.2. Effects of convective regime on plume heat flow

To clarify how plume heat flow  $Q_p$  depends on the convective regimes, we estimated  $Q_p$  for the cases E1 to E7 shown in Fig. 2; we controlled the convective regimes by changing the magnitude of temperature-dependence of viscosity  $E$ . The internal heating rate  $H=0.0$  for all of the cases.

Fig. 4 shows the plots of the basal heat flow  $Q_b$ , the plume heat flow  $Q_p$ , and the ratio of plume heat flow to basal heat flow  $\gamma_{pb} \equiv Q_p/Q_b$ , all against  $E$ . The plume heat flow  $Q_p$  is only about 30% of the basal heat flow  $Q_b$  and both  $Q_p$  (Fig. 4a) and the heat flow ratio  $\gamma_{pb}$  (Fig. 4b) do not significantly depend on  $E$  in the plate-like regime. Outside of the plate-like regime, however,  $\gamma_{pb}$  increases as  $E$  moves away from the range for the plate-like regime. The ratio  $\gamma_{pb}$  is as high as 40–70% in both the weak plate and stagnant lid regimes in the range of  $E$  studied here (Fig. 4b). The ratio  $\gamma_{pb}$  increases with decreasing  $E$  in the weak plate regime because  $Q_p$  becomes larger as a result of increasing  $\Delta T_{\text{plume}}$ , while  $\gamma_{pb}$  increases with increasing  $E$  in the stagnant lid regime because  $Q_b$  decreases with increasing  $E$  (Fig. 4a).

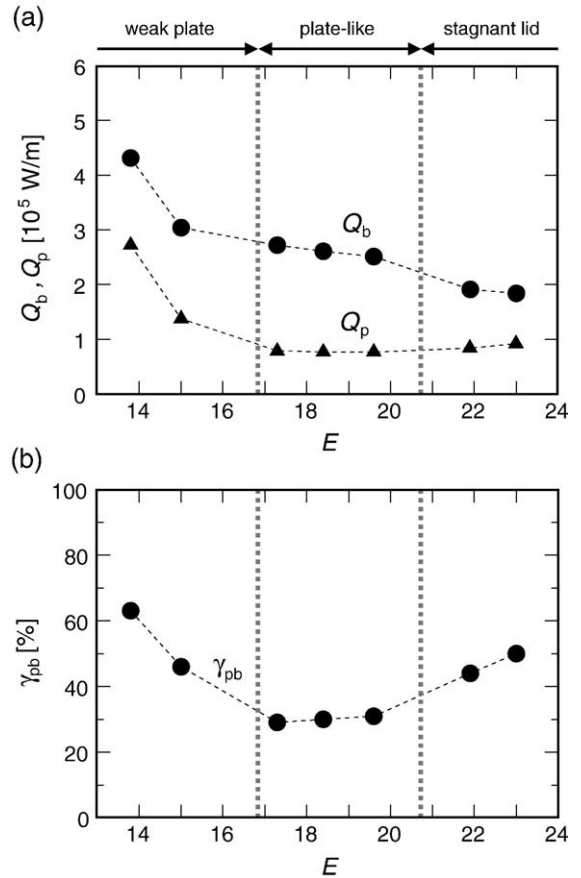


Fig. 4. Plots of directly estimated plume heat flow for cases E1–E7 shown in Fig. 2. (a) The magnitude of temperature dependence of viscosity  $E$  versus the plume heat flow ( $Q_p$ , solid triangles) and bottom surface heat flow ( $Q_b$ , solid circles). (b)  $E$  versus the ratio of the plume heat flow to the bottom surface heat flow ( $\gamma_{pb}$ , solid circles). Dashed lines in both figures indicate the regime boundaries of convective flow pattern shown in Fig. 2.

#### 4.2.3. Plume heat flow estimated by plume-swell

We now present, in Fig. 5a, the plots of plume heat flow estimated by topographic plume-swells  $Q_s$  (see Eq. (10)), the ratio of  $Q_s$  to basal heat flow ( $\gamma_{sb} \equiv Q_s/Q_b$ ), the ratio of  $Q_s$  to top surface heat flow ( $\gamma_{st} \equiv Q_s/Q_t$ ) and the ratio of  $Q_s$  to real plume heat flow estimated in the previous section ( $\gamma_{sp} \equiv Q_s/Q_p$ ), all against  $H$  for the cases H1 to H4 in the plate-like regime (see Fig. 2). The swell height  $\delta h_{\text{swell}}$  in Eq. (10) is defined by the difference between the maximum dynamic topography on the plume-swells and dynamic topography at the edge of plume-swells and the dynamic topography is computed by  $\delta h_{\text{top}} = \sigma_{zz}|_{z=1} / \Delta\rho_{\text{top}}g$  where  $\sigma_{zz}|_{z=1}$  is the normal stress at the top boundary (e.g., [35]) as usual. The estimates of plume heat flow in Fig. 5a are calculated as an average of estimates from several snapshots of convective flow pattern during each run.

The plume heat flow estimated by plume-swells is only a few percent of basal heat flow (see  $\gamma_{sb}$  in Fig. 5a), and is not more than 10% of real plume heat flow (see  $\gamma_{sp}$  in Fig. 5a) for all of the cases. This occurs

because the basic assumption for the estimate of  $Q_s$ , i.e., the flux of buoyancy supplied to the asthenosphere beneath plume-swells by hot upwelling plumes being equal to the flux of buoyancy taken away from the plume-swells by moving plates, does not hold for our model. As shown in Fig. 5b, the heads of hot upwelling plumes laterally spread out beneath the lithosphere at a velocity higher than the plate velocity by an order of magnitude in our model. The laterally spreading plume heads, therefore, largely take the buoyancy supplied to the asthenosphere beneath plume-swells away. Namely, the buoyancy flux of hot upwelling plumes is largely underestimated when calculated from the amplitude of plume-swell and this is the reason for the low  $\gamma_{sp}$  observed in Fig. 5a (see also [33]).

We also confirmed, from a similar analysis of cases E3 to E5 shown in Fig. 2, that  $\gamma_{sb}$  and  $\gamma_{sp}$  do not significantly depend on the magnitude of temperature-dependence of viscosity  $E$  in the plate-like regime. (In the weak plate regime, however, we found that  $\gamma_{sp}$  and  $\gamma_{st}$  become significantly higher than the values shown

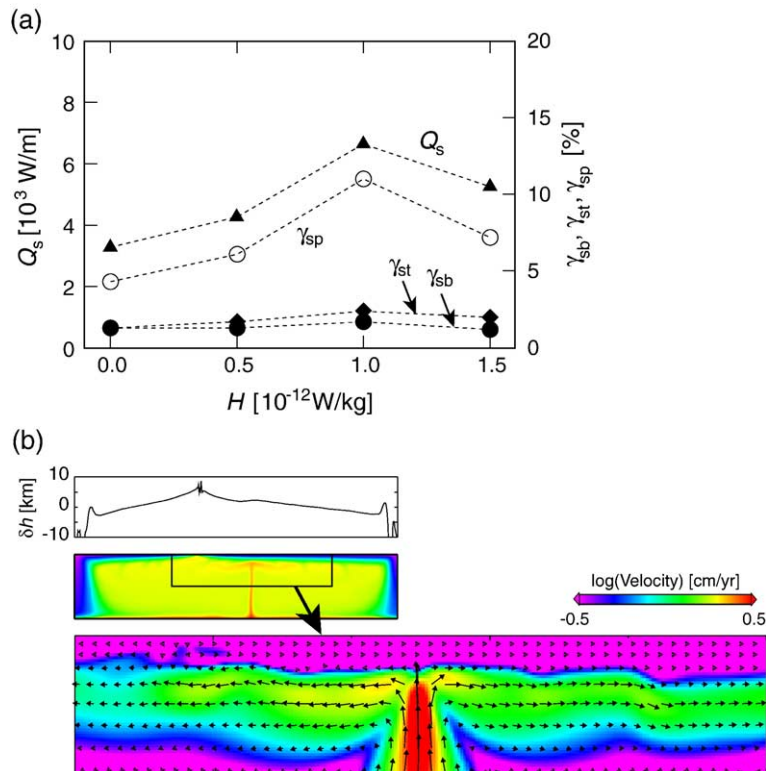


Fig. 5. (a) Plots of plume heat flow estimated by plume-swell for cases H1–H4 shown in Fig. 2. The plume heat flow ( $Q_s$ , solid triangles), the ratio of the plume heat flow to the heat flow on the bottom boundary ( $\gamma_{sb}$ , solid circles), the ratio of the plume heat flow to the heat flow on the top boundary ( $\gamma_{st}$ , solid diamonds), and the ratio of the plume heat flow estimated by the plume-swell ( $Q_s$ ) to the real plume heat flow (see Fig. 3) ( $\gamma_{sp}$ , open circles) are plotted against internal heating rate  $H$ . (b) The temperature field for case H1 (the same as Fig. 2c), the calculated dynamic topography, and the velocity field around the head of the upwelling plume.

in Fig. 5a, though an accurate estimate of  $\gamma_{sp}$  and  $\gamma_{st}$  is difficult in this regime.)

## 5. Residual topography

The residual topography, the difference between the real topography and the topography expected from the half-space cooling model of oceanic plates, has been estimated for the Earth [36,37]; the residual topography is 0.5–1.0 km over the “super-swells” on the South Pacific (e.g., [4,38]). For comparison, we present the plots of residual topography for cases H1 to H4 in the plate-like regime (see Fig. 2) in Fig. 6. Here, the residual topography is calculated as

$$\delta h_{res} = \delta h - d_b, \quad (11)$$

where  $\delta h$  is the dynamic topography, and  $d_b$  is depth of ocean floor calculated from the half-space cooling model [4,39]. Namely,  $d_b$  is calculated as

$$d_b \equiv d_0 + \frac{2\rho_m \alpha_0 (T_m - T_0)^2}{\pi(\rho_m - \rho_w)} \frac{1}{q_t}, \quad (12)$$

where  $q_t$  is the heat flow estimated on the surface,  $d_0$  the depth of ridge crest,  $\rho_m$  mantle density,  $\rho_w$  ocean water density,  $T_m$  mantle temperature, and  $T_0$  is surface temperature. Eq. (11) implies that, when hot upwelling plumes and other hot materials do not exist beneath the lithosphere, the residual topography  $\delta h_{res}$  should become zero. In our numerical result, we confirmed that  $\delta h_{res}$  really tends to zero on the upstream side of plumes away from the plumes (see the left part of Fig. 6).

Fig. 6 shows that the residual topography is about 2.5 km over the upwelling plume when  $\gamma_{bt}=100\%$  (complete basal heating), while the residual topography is about 0.5 km when  $\gamma_{bt}=57\%$ . The residual topography of 0.5–1.0 km observed for the Earth occurs in our model when the proportion of basal heating to the total heating  $\gamma_{bt}$  is 50–70%.

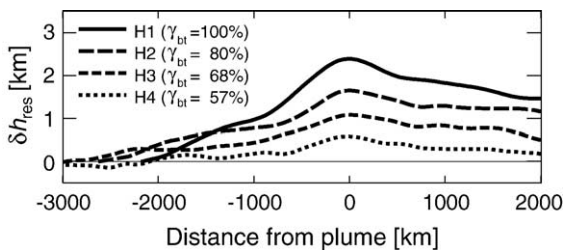


Fig. 6. The calculated residual topography for cases H1–H4 shown in Fig. 2. The horizontal axis represents the dimensional distance from the top of plume. The ratios of plume heat flow to bottom surface heat flow ( $\gamma_{pb}$ ) in the figure are taken from Fig. 3b.

## 6. Discussion and conclusions

The most important result of the present numerical experiments is that plume heat flow is only a small fraction, less than 30%, of the heat flux at the bottom of the convecting layer in the plate-like regime; the rest is used for warming up the subducted slabs that lay on the bottom boundary. The fraction of plume heat flux is significantly lower in the plate-like regime than in the weak plate regime. Namely, the fraction significantly depends on the convective regimes and it is precarious to draw conclusions on plume heat flow from the numerical experiments where the convective regime is not carefully controlled.

The small fraction of plume heat flow in the plate-like regime suggests that the low plume heat flow observed on the Earth does not necessarily imply that the basal heating is not important in driving the Earth’s mantle convection in contrast to the earlier suggestions (e.g., [5]). The heat flow at the bottom boundary is most likely much higher than the observed plume heat flow partly because a large portion of the bottom heat flow is most likely used for heating up the subducted slabs that are suggested to lay in the deep lower mantle (e.g., [40]). Furthermore, when calculated from the amplitude of plume-swells as in [2,3], the plume heat flow may be significantly underestimated since a large portion of buoyancy transported by hot upwelling plumes may be taken away from the asthenospheric regions beneath plume-swells by laterally spreading plume heads in the asthenosphere instead of moving plates as observed in our model. Indeed, a recent high-resolution tomographic image [41] suggests a significant amount of heat from the superplumes in the deep lower mantle is carried horizontally in the asthenosphere. It may be just a coincidence that the plume heat flow is comparable to the heat flow at the core–mantle boundary suggested from the studies of geodynamo [6] and the thermal history of the core [7–9] on the Earth.

Though the basal heating rate is difficult to quantitatively estimate from plume heat flow by the reason described above, the present numerical experiments do suggest that the plume heat flow and the amplitude of hotspot-swells observed on the Earth can be more easily understood if the convecting part of the mantle is strongly heated from its bottom boundary. The fraction of plume heat flow to the surface heat flow and the amplitude of topographic high comparable to those of hotspot-swells observed for the Earth are obtained in the numerical models when the fraction of basal heating to the total heating is as high as 50–70% (see Figs. 5a and 6).

This high fraction of basal heating is difficult to realize if the bottom boundary of the convecting mantle is the core–mantle boundary even if the core contains a strong internal heat source as suggested from the studies of the core’s thermal history [6,9]. The “bottom boundary” may, at least partly, correspond to the boundary of the regions in deep lower mantle occupied by materials enriched in heat producing elements as suggested from a tomographic image and the thermal budget of the mantle [11,14], though the enriched regions may not be a continuous layer originally suggested [42]. The hot plumes in the Earth’s mantle may be coming from the undulating boundary of such deep enriched regions [15] instead of a horizontal boundary assumed in the present numerical experiments or, more generally from any chemically distinct regions with stronger internal heat source [43]. Further quantitative study is necessary to estimate the fraction of plume heat flow to “basal” heating rate in the Earth’s mantle.

## Acknowledgments

We thank Dr. Allen K. McNamara and two anonymous reviewers for their thoughtful comments. We thank Prof. P.J. Tackley for providing us his convection code `stag3d`. Calculations were carried out on the computer facilities of the Earthquake Information Center, Earthquake Research Institute (ERI), University of Tokyo. M.Y. was financially supported by the Japan Society for the Promotion of Science (JSPS) Research Fellowship at ERI from 2000 to 2003. This study was partly supported by the Grand-in-Aid for Scientific Research (JSPS Fellows, #12-01228) from the Ministry of Education, Culture, Sports, Science and Technology, Japan.

## References

- [1] W.J. Morgan, Convection plumes in the lower mantle, *Nature* 230 (1971) 42–43.
- [2] G.F. Davies, Ocean bathymetry and mantle convection: 1. Large-scale flow and hotspots, *J. Geophys. Res.* 93 (1988) 10467–10480.
- [3] N.H. Sleep, Hotspots and mantle plumes: some phenomenology, *J. Geophys. Res.* 95 (1990) 6715–6736.
- [4] G.F. Davies, *Dynamic Earth: Plates, Plumes and Mantle Convection*, Cambridge Univ. Press, Cambridge, UK, 1999, 458 pp.
- [5] G.F. Davies, M.A. Richards, *Mantle convection*, *J. Geol.* 100 (1992) 151–206.
- [6] B.A. Buffett, The thermal state of Earth’s core, *Science* 299 (2003) 1675–1677.
- [7] B.A. Buffett, H.E. Huppert, J.R. Lister, A.W. Woods, Analytical model for solidification of the Earth’s core, *Nature* 356 (1992) 329–331.
- [8] B.A. Buffett, Dynamics of the Earth’s core, in: S. Karato, A. Forte, R. Liebermann, G. Masters, L. Stixrude (Eds.), *Earth’s Deep Interior: Mineral Physics and Tomography From the Atomic to the Global Scale*, Am. Geophys. Union, Geophys. Monogr., vol. 117, 2000, pp. 37–62.
- [9] S. Labrosse, Thermal and magnetic evolution of the Earth’s core, *Phys. Earth Planet. Inter.* 140 (2003) 127–143.
- [10] B.L.N. Kennett, S. Widiyantoro, R.D. van der Hilst, Joint seismic tomography for bulk sound and shear wave speed in the Earth’s mantle, *J. Geophys. Res.* 103 (1998) 12469–12493.
- [11] R.D. van der Hilst, H. Kárason, Compositional heterogeneity in the bottom 1000 kilometers of Earth’s mantle: toward a hybrid convection model, *Science* 283 (1999) 1885–1888.
- [12] M. Ishii, J. Tromp, Normal-mode and free-air gravity constraints on lateral variations in velocity and density of Earth’s mantle, *Science* 285 (1999) 1231–1236.
- [13] J. Trampert, F. Deschamps, J. Resovsky, D. Yuen, Probabilistic tomography maps chemical heterogeneities throughout the lower mantle, *Science* 306 (2004) 853–856.
- [14] L.H. Kellogg, B.H. Hager, R.D. van der Hilst, Compositional stratification in the deep mantle, *Science* 283 (1999) 1881–1884.
- [15] A. Davaille, Simultaneous generation of hotspots and super-swells by convection in a heterogeneous planetary mantle, *Nature* 402 (1999) 756–760.
- [16] A.M. Jellinek, M. Manga, The influence of a chemical boundary layer on the fixity and lifetime of mantle plumes, *Nature* 418 (2002) 760–763.
- [17] A.M. Jellinek, M. Manga, Links between long-lived hotspots, mantle plumes,  $D''$ , and plate tectonics, *Rev. Geophys.* 42 (2004) RG3002, doi:10.1029/2003RG000144.
- [18] S. Labrosse, Hotspots, mantle plumes and core heat loss, *Earth Planet. Sci. Lett.* 199 (2002) 147–156.
- [19] E.L. Mittlestaedt, P.J. Tackley, Plume heat flow is much less than CMB heat flow, Fall Meet. Suppl., Abstract T21A-0869, *EOS Trans. AGU*, vol. 82, 2001.
- [20] S. Zhong, Plume heat flux, core heat flux, and the style of mantle convection, Fall Meet. Suppl., Abstract T42A-02, *EOS Trans. AGU*, vol. 85, 2004.
- [21] V. Courtillot, A. Davaille, J. Besse, J. Stock, Three distinct types of hotspots in the Earth’s mantle, *Earth Planet. Sci. Lett.* 205 (2003) 295–308.
- [22] R. Montelli, G. Nolet, F.A. Dahlen, G. Masters, E.R. Engdahl, S.-H. Hung, Finite-frequency tomography reveals a variety of plumes in the mantle, *Science* 303 (2004) 338–343.
- [23] M. Ogawa, Plate-like regime of a numerically modeled thermal convection in a fluid with temperature-, pressure-, and stress-history-dependent viscosity, *J. Geophys. Res.* 108 (2003) 2067, doi:10.1029/2000JB000069.
- [24] D. Bercovici, Generation of plate tectonics from lithosphere-mantle flow and void-volatile self-lubrication, *Earth Planet. Sci. Lett.* 154 (1998) 139–151.
- [25] P.J. Tackley, Self-consistent generation of tectonic plates in time-dependent, three-dimensional mantle convection simulations: 2. Strain weakening and asthenosphere, *Geochem. Geophys. Geosyst.* 1 (2000), doi:10.1029/2000GC000043.
- [26] W.R. Peltier, Postglacial variations in the level of the sea—implications for climate dynamics and solid-earth geophysics, *Rev. Geophys.* 36 (1998) 603–689.
- [27] S.D. King, Models of mantle viscosity, in: T.J. Ahrens (Ed.), *Mineral Physics and Crystallography: A Handbook of Physical Constants*, Amer. Geophys. Union, Washington, DC, 1995, pp. 227–236.

- [28] D.L. Kohlstedt, B. Evans, S.J. Mackwell, Strength of the lithosphere—constraints imposed by laboratory, *J. Geophys. Res.* 100 (1995) 17587–17602.
- [29] H. Kanamori, D. Anderson, Theoretical basis of some empirical relations in seismology, *Bull. Seismol. Soc. Am.* 65 (1975) 1073–1095.
- [30] P.J. Tackley, Effects of strongly variable viscosity on three-dimensional compressible convection in planetary mantles, *J. Geophys. Res.* 101 (1996) 3311–3332.
- [31] G. Schubert, D.L. Turcotte, P. Olson, *Mantle Convection in the Earth and Planets*, Cambridge Univ. Press, Cambridge, UK, 2001, 940 pp.
- [32] D.L. Turcotte, G. Schubert, *Geodynamics*, Second edition, Cambridge Univ. Press, Cambridge, UK, 2002, 456 pp.
- [33] N.M. Ribe, U.R. Christensen, Three-dimensional modeling of plume–lithosphere interaction, *J. Geophys. Res.* 99 (1994) 669–682.
- [34] R.G. Gordon, Diffuse oceanic plate boundaries: strain rates, vertically averaged rheology, and comparisons with narrow plate boundaries and stable plate interiors, in: M. Richards, G. Gordon, R.D. van der Hilst (Eds.), *The History and Dynamics of Global Plate Motions*, Am. Geophys. Union, Geophys. Monogr., vol. 121, 2000, pp. 143–159.
- [35] M.A. Richards, B.H. Hager, Geoid anomalies in a dynamic Earth, *J. Geophys. Res.* 89 (1984) 5987–6002.
- [36] M. Kido, T. Seno, Dynamic topography compared with residual depth anomalies in oceans, *Geophys. Res. Lett.* 21 (1994) 717–720.
- [37] M. Gurnis, J.X. Mitrovica, J. Ritsema, H.-J. van Heijst, Constraining mantle density structure using geological evidence of surface uplift rates: the case of African Superplume, *Geochem. Geophys. Geosyst.* 1 (2000), doi:10.1029/1999GC000035.
- [38] M.K. McNutt, Superswells, *Rev. Geophys.* 36 (1998) 311–344.
- [39] G.F. Davies, Role of the lithosphere in mantle convection, *J. Geophys. Res.* 93 (1988) 10451–10466.
- [40] C. Lithgow-Bertelloni, M.A. Richards, The dynamics of Cenozoic and Mesozoic plate motions, *Rev. Geophys.* 36 (1998) 27–78.
- [41] B. Romanowicz, Y. Gung, Superplumes from the core–mantle boundary to the lithosphere: implications for heat flux, *Science* 296 (2002) 513–516.
- [42] P.J. Tackley, Mantle convection and plate tectonics: toward an integrated physical and chemical theory, *Science* 288 (2000) 2002–2007.
- [43] M. Ogawa, Chemical stratification in a two-dimensional convecting mantle with magmatism and moving plates, *J. Geophys. Res.* 108 (2003) 2561, doi:10.1029/2002JB002205.